

Dynamic breakup of Janus droplet in a bifurcating microchannelHao Wang , Shiteng Wang, Yao Mu, Qing Han, and Yi Cheng**Department of Chemical Engineering, Tsinghua University, Beijing 100084, People's Republic of China*

(Received 17 January 2024; accepted 6 May 2024; published 11 June 2024)

Droplet breakup is frequently observed in natural and industrial processes and has been considered as a promising approach for increasing productivity and adjusting droplet size in the microfluidic production of emulsions. Although valuable insights on the breakup mechanisms of single-phase droplets in microchannels have been provided over the past decades, the breakup physics of complex emulsions is still poorly understood. Spatially asymmetric Janus microdroplets, distinct from single-phase or double emulsion droplets possessing one uniform interface with the ambient phase, are anticipated to show unique breakup behaviors, which has not been explored. Here, we conduct both microfluidic experiments and three-dimensional lattice Boltzmann simulations to investigate the dynamic breakup of ionic liquid (IL)-water Janus droplets in an assembled 3D-printed microchannel with a bifurcation. Three different flow regimes are identified: (i) division into two daughter Janus droplets, (ii) breakup into a single-phase droplet and a smaller Janus droplet, and (iii) nonbreakup. A map of the breakup modes of Janus droplets is constructed based on the average capillary numbers (Ca_{av}) of the continuous phase and the normalized droplet equivalent diameters. We find that the strong constraint effect of the main channel and large Ca_{av} values are essential to the symmetrical breakup of Janus droplets. The tunnel between the mother droplet and the wall of the main channel, which allows the lateral shift of the Janus droplet, and moderate flow rates facilitate the breakup of the IL single-phase portion of Janus droplets. Through 90° rotation of the splitting microchannel, we elucidate the distinctions in Janus droplet behaviors under two baffle orientations. Potential impacts of the oblique flow characteristic of [bmim]FeCl₄-water Janus droplets on the droplet breakup are discussed.

DOI: [10.1103/PhysRevFluids.9.064203](https://doi.org/10.1103/PhysRevFluids.9.064203)**I. INTRODUCTION**

Droplet-based microfluidics has been vastly utilized to prepare and manipulate complex emulsions in chemical and biological research fields, owing to its advantages of precise control over the size, morphology, and composition of submicroliter droplets [1–6]. However, one technical shortcoming originating from the small-volume feature of microfluidics is the low droplet production rate, generally less than one hundred to a few thousand hertz per microchannel (volume throughput no more than dozens of liters per year for each channel) [7], which limits the industrial applications for the microfluidic production of complex droplets. And droplet makers for complex emulsions, including Janus droplets and multiple emulsions, typically need patterned wettability or multistage junctions [8–10]. Thus, the direct parallelization of these identical droplet generators makes the fabrication of microdevices more challenging and expensive.

Droplet breakup is a simple and flexible approach to increasing droplet yields and further adjusting droplet sizes without entirely relying on droplet makers, which has become an important

*Corresponding author: yicheng@tsinghua.edu.cn

research branch of microfluidics [11–13]. Reported droplet splitting approaches can be categorized into passive or active methods according to whether external force fields are involved. Various confined geometries, such as two-dimensional (2D) T [14–17] or Y [18,19] junctions, obstacles [14,20–22], three-dimensional (3D) multipore glass capillary [23,24], bifurcated [25–27], or constricted [28–31] structures, and even the interface between immiscible multiphases [32], could achieve the passive breakup of droplets. While active approaches usually adopt electric [33], acoustic [34], and magnetic fields [35] to assist droplet breakup, many of these studies still rely on the passive method and need to introduce geometrical constraints. Practically, the passive breakup of complex droplets is commonly observed in real applications when the droplets as products encounter obstacles or baffles or go through a porous structure during production and transportation operations. Therefore, a thorough understanding of the passive breakup of complex droplets in microchannels is strongly required for the large-scale production and actual applications of the microfluidic preparation of complex emulsions.

However, studies of the passive breakup of complex emulsions are quite limited compared to the extensive research on the breakup of single-phase droplets in microdevices. Only a few works have been carried out on the breakup of double emulsions [23,36–39]. As ground-breaking research, Abate and Weitz [36] successfully achieved three-time continuous breakup of double emulsions via a splitting array with repeated Y junctions and obtained final droplets in tens of microns with a coefficient of variation (CV) of 6%. They demonstrated that the splitting of double emulsions follows a two-stage process similarly observed in that of single droplets. Chen *et al.* [23] designed a three-dimensional splitting microdevice which splits one double droplet with a core-shell structure into two or three portions via multipore glass capillaries. The sizes of their daughter droplets are several hundreds of micrometers with a low CV of less than 3%. To investigate permeation behaviors of double emulsions, Akamatsu *et al.* [37] fabricated a two-dimensional PDMS microchannel with linear segmentation obstacles to mimic membrane pores. They revealed the probabilities of each breakup mode under different flow rates and observed the breakup of a double emulsion droplet into a smaller double emulsion droplet and a single-phase droplet of the shell phase. Liu *et al.* [39] presented a new classification of breakup regimes of double emulsions at a Y-shaped bifurcation based on whether contacts between the core and shell interfaces of double emulsion droplets are observed during breakup processes. Unlike only one interface of the core-shell multiphase emulsions being formed with the ambient phase, Janus droplets, named after the ancient two-faced Roman god, possess two or more surfaces with different physical or chemical properties [40,41]. These droplets have attracted increasing attention from researchers recently due to their great potential as color displays [4,42,43], catalysts [44], drug carriers [45], microextractors [46], and reactors [47,48]. Conceivably, the anisotropic nature of Janus droplets makes their hydrodynamic behaviors at the microscale more complicated compared to single or double emulsions. To our knowledge, no work has investigated the breakup of Janus droplets in microchannels.

To capture and quantify flow characteristics of complex droplet flow at such small scales of time and space, it is difficult to merely count on experimental approaches, especially in three-dimensional microdevices. Numerical simulations could greatly benefit the study of complex droplet behaviors and provide detailed information such as dynamic deformation of multiphase interfaces, pressure distributions, and velocity fields. Both classical computational fluid dynamics methods and mesoscopic models have been applied to study the breakup of complex emulsions in microchannels. Yu *et al.* [49] used a ternary phase volume of fluid (VOF) model to present the evolutions of velocity and pressure fields during the breakup of double emulsions in a Y-junction microchannel. Zhou *et al.* [50] performed 2D numerical simulations based on the finite element method to investigate a single-phase droplet breakup regime driven by interfacial tension in a T-junction geometry. In essence, the macroscopic phase separation and interfacial dynamics emanate from the microscopic interparticle forces or interactions. Hence, mesoscopic models are preferable to deal with such problems. The lattice Boltzmann method (LBM), based on the Boltzmann equation and kinetic theory, has become a promising numerical tool to study multiphase, multicomponent flows at microscale [51], such as the generation [52,53], breakup [54], deformation [55], coalescence [56], and mixing [57,58]

of microdroplets, owing to its inherent advantages in tracking moving deformable interfaces and dealing with complex boundaries with high numerical stability. In our previous work, a ternary color-gradient lattice Boltzmann (LB) model was established to predict morphologies of three-phase emulsions and investigate the formation of double emulsions and Janus droplets in microchannels in 2D simulations [59–61]. However, the 2D simulation of Janus droplets only considers the flows in the central plane of the microchannel and ignores the cross-section information. Later, in order to depict the flow behaviors of Janus droplets more accurately, we further developed the model into a 3D one to study the generation of Janus droplets and demonstrate the collapsing process of Janus dispersed thread [62]. Zhou *et al.* [63] recently reported a 2D color-gradient LB simulation of double emulsions penetrating a constricted structure without breakup.

In this work, the dynamic breakup of ionic liquid (IL)-water Janus droplets in a bifurcating microchannel is investigated. 3D LBM simulations are performed to explain the experimental observations and reveal the evolution of the pressure and velocity vector fields during droplet breakup via the ternary color-gradient model. Three distinct flow regimes of Janus droplet passing through the breakup microchannel are characterized, and the feature of the oblique flow of [bmim]FeCl₄-water Janus droplets induced by the different hydrodynamic resistances between two semidroplets in the main channel is pointed out. We consider, in particular, important factors that might influence the breakup of Janus droplets. Based on the normalized equivalent diameters of Janus droplets and the Ca_{av} numbers of the continuous phase, transitions between two breakup regimes are identified, and the effect of the bifurcation orientation on the breakup of Janus droplets is demonstrated.

II. EXPERIMENTAL METHODS

A. Assembled 3D-printed microchannel

The formation and breakup of Janus droplets are performed in an assembled 3D-printed microdevice, as shown in Fig. 1(a). All the 3D-printed modules are designed via the commercial software Solidworks (Dassault Systemes S.A.), then fabricated by Stratasys Polyjet™ printer (EDEN 260VS™) using a transparent photopolymer (VeroClear™). Janus droplets are produced using a 30 mm × 20 mm × 5 mm assembled droplet generator [module I in Fig. 1(a)] based on a coflow method. Two vertical channels of the 3D-printed fitting for continuous phase injection are equal with diameters of 0.8 mm and a theta capillary with originally 1.5-mm outer diameter, which is tapered by a micropipette puller (P-97, SUTTER Co. Ltd., USA) to form binozzles with approximately 50-μm inner diameters, is inserted into the cross channel of the 3D-printed fitting for two dispersed flows. To prevent swelling of the resin and avoid the effect of the residual support materials staying on the wall of the 3D-printed microchannel, a transparent polytetrafluoroethylene (PTFE) plastic tube with 0.8-mm inner diameter served as the main channel, and it also connects the droplet generator to a 20 mm × 12 mm × 2.2 mm droplet splitting module, shown as module II in Fig. 1(a). Two different baffle orientations of the bifurcating microchannels are designed to investigate the breakup behaviors of Janus droplets, as shown in Figs. 1(b1) and 1(c1) and Figs. 1(b2) and 1(c2). Two PTFE tubes with inner diameter of 0.6 mm are inserted into and tightly fitted with the 3D-printed element. For good coaxiality, the outer diameters of tubes are matched with the inner dimensions of the 3D-printed modules.

B. Experimental setup and materials

A typical ternary liquid system, as listed in Table I, is introduced to produce Janus droplets without adding any surfactants, which is an ideal system to investigate the droplet breakup process. 1-Butyl-3-methylimidazolium tetrachloroferrate ([bmim]FeCl₄, purchased from Dibo Chemical Technology Co., Ltd. Shanghai, China), which is an IL with magnetic properties, and water served as the dispersed phases (DPs). Soybean oil (Aladdin Co., Ltd) is used as the continuous phase (CP) to generate [bmim]FeCl₄-water Janus droplets. Fluids were injected into microchannels separately by syringe pumps (Baoding Longer Precision Pump Co., Ltd, Beijing, China). After allowing a

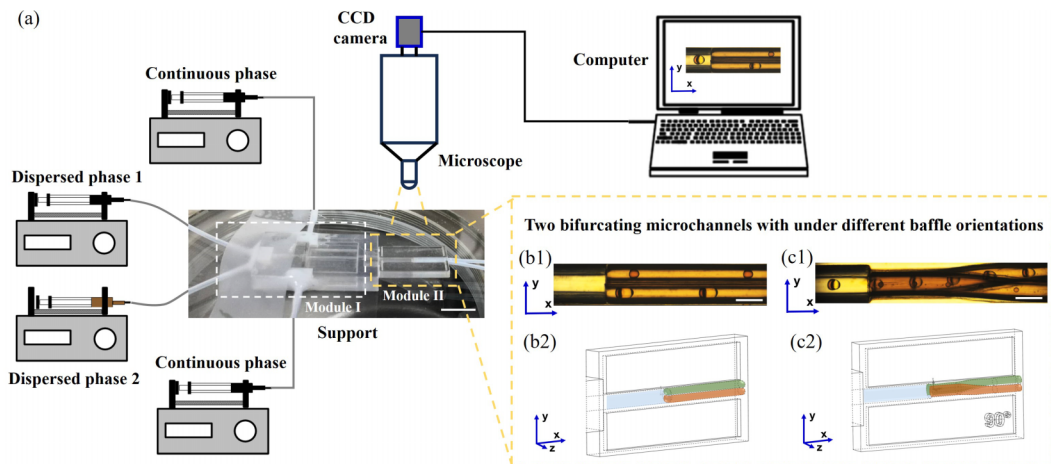


FIG. 1. (a) The diagram of the experimental setup. Assembled 3D-printed microchannels on the support are utilized for the generation and breakup of Janus droplets. Module I is an assembled coaxial generator of Janus droplets, where two vertical branch channels are used for the injection of the continuous phase and two dispersed phases are pumped into the cross channels. Module II is the splitting microchannel. Scale bar is 10 mm. Two bifurcating microchannels are employed: one features a baffle between two subchannels which is vertical to the view plane of the microscope (the x - y plane) as depicted in (b1) the experimental micrograph and (b2) the 3D schematic diagram. Scale bar is $1000\ \mu\text{m}$. The other microchannel is obtained by rotating the former bifurcation by 90° , causing the baffle to align parallel to the x - y plane, as shown in (c1) the experimental micrograph and (c2) the 3D schematic diagram. And, in the latter microchannel, the rear of the top subchannel is repositioned as the lower branch at the x - y plane, and the end of the bottom subchannel is shifted to the x - y plane as the upper branch through 3D printing manufacture, facilitating direct observation on the view plane of the microscope. Scale bar is $1000\ \mu\text{m}$. In the 3D schematic diagrams (b2) and (c2), the main channel is delineated in blue, while the two subchannels are marked in green and orange, respectively.

few minutes for the system to reach a steady state, to check the hydrodynamic resistances of the two subchannels, the flow rate of the continuous phase Q_c , is set relatively low at $25\ \mu\text{L}/\text{min}$. The flow rates of the two dispersed phases are both $15\ \mu\text{L}/\text{min}$ each, resulting in the generation of Janus droplets that flow as plugs, fully obstructing the channel. Then, after observing the stable division of Janus droplets into two similar daughter Janus droplets flowing at the same steps in the subchannels, we continuously collected the daughter Janus droplets in a given time for size measurement. It turns out that, in each subchannel, the number of collected daughter droplets is identical, and the average sizes of the daughter droplets are quite close (the detailed analysis of the sizes of daughter Janus droplets is provided in the Supplemental Material [64]). Thus, the difference in hydrodynamic resistance for the subchannels is negligible. The breakup process of

TABLE I. Fluid properties in experiments and corresponding parameters in lattice units for subsequent LB simulations.

Continuous phase (CP) or dispersed phase (DP)	Fluid density		Kinematic viscosity		Interfacial tension, σ	
	Physical units (kg/m^3)	Lattice units	Physical units ($\text{mPa}\cdot\text{s}$)	Lattice units	Physical units (mN/m) [65]	Lattice units
CP: Soybean oil	0.92×10^3	1.0	8.5	0.1	$\sigma_{\text{DP1-2}} = 15$	0.015
DP1: [bmim]FeCl ₄	1.4×10^3	1.0	31	0.3	$\sigma_{\text{CP-DP1}} = 14$	0.014
DP2: Water	1.0×10^3	1.0	1.0	0.01	$\sigma_{\text{CP-DP2}} = 23$	0.02

Janus droplets is recorded by a high-speed color CCD camera (edge 5.5, PCO GmbH, Germany), which is connected to the microscope (Nikon, MM400/L), at a shooting frame rate of 200–500 frames per second (fps). Size measurement is conducted via EMAX software.

III. NUMERICAL MODEL OF THREE-DIMENSIONAL MULTIPHASE, MULTICOMPONENT LATTICE BOLTZMANN METHOD

A. Algorithm of 3D ternary color-gradient lattice Boltzmann model

The computational framework of the current 3D color-gradient LB model is presented in Table II. The present model, which incorporates the multiphase collision operators proposed by Leclaire *et al.* [66], has been proven to be capable of dealing with immiscible multiphase flows for large viscosity ratios up to $O(100)$ at unit density ratio. In LBM, the hydrodynamic behaviors of flows are captured through local microscale operations where fluids are assumed to be discretely fictitious particles performing alternate steps of collision and streaming along discretized lattice directions. This whole process can be expressed by the evolution of the particle distribution function (PDF) $f_i^k(\mathbf{x}, t)$, as described by Eq. (1) in Table II. For ternary flows, three sets of PDFs should be introduced, and the typical D3Q19 discretized scheme (3 dimensions and 19 discrete momenta) [67] is adopted for 3D simulations. As shown in Eq. (2), a collision operator Ω_i^k is defined to represent the local redistribution of PDFs due to collisions, which consists of three operators [66]. One collision operator to start with, based on the Bhatnagar-Gross-Krook (BGK) approximation, is the BGK operator $(\Omega_i^k)^1$, which is adopted to achieve the momentum exchange in single-phase fields [68]. It expresses the relaxation of the PDF toward the equilibrium distribution $f_i^{k(\text{eq})}(\mathbf{x}, t)$ with a single relaxation time, which determines the equilibration speed [67,68], as expressed by Eqs. (3)–(6). The relaxation time is related to the kinematic viscosity of fluids as given in Eq. (17). Then, to describe multiphase flows, multiphase collision operators composed of a perturbation operator $(\Omega_i^k)^2$ and a recoloring operator $(\Omega_i^k)^3$ are introduced. The $(\Omega_i^k)^2$ is defined as Eq. (7) to generate the interfacial tension through exerting a color-gradient force [expressed as Eq. (8)] across the interface with respect to Laplace law, Young-Laplace law, and isotropy of the interface [66]. The $(\Omega_i^k)^3$ is used to maintain interfaces with a reasonable thickness and satisfy the conservation laws of mass and momentum [69], as expressed by Eqs. (11)–(13). After a collision procedure, the PDF of phase k in the i th direction at lattice site \mathbf{x} and moment t , $f_i^k(\mathbf{x}, t)$, streams to the neighboring site with lattice velocity \mathbf{e}_i and turns into $f_i^k(\mathbf{x} + \mathbf{e}_i\delta t, t + \delta t)$ at the next time step $t + \delta t$ as shown in Eq. (1). With increasing the time step (t.s.), operations of collision and streaming are alternately repeated until the convergence has been reached. Macroscopic quantities could be calculated by Eqs. (14)–(16) through moment integrations of PDFs.

B. Problem description

LB simulations are carried out in the lattice system where the physical properties in SI units are necessarily mapped to the lattice in lattice units. Table I shows the physical parameters in the [bmim]FeCl₄-water/soybean oil system and counterparts in lattice units (l.u.). In the present simulations, three phases, [bmim]FeCl₄, water, and soybean oil, are represented by blue, red, and transparent fluids. As displayed in Figs. 2(a) and 2(b), the [bmim]FeCl₄-water Janus droplet has a dumbbell structure in the bulk phase of soybean oil, and the numerical results agree well with the experimental ones. The water droplet is partially engulfed by the IL semidroplet. We adopted the same definition of the Janus droplet size, i.e., the equivalent diameter of Janus droplet, D_e , as in the literature, where D_e is the maximum diameter between two droplet pairs observed in the dumbbell Janus structure [40]. The ability of the 3D ternary color-gradient LB model to accurately simulate the contact morphologies of three-phase emulsions was quantitatively and systematically validated in our previous work [62]. To model the breakup of the Janus droplet, the setup of the splitting microchannel is illustrated in Fig. 2(c). The x - y plane in the numerical simulations corresponds

TABLE II. The computational framework of the 3D ternary color-gradient LB model.

Fundamental operations	Descriptions	Equations
Evolution scheme: collision and streaming	The distribution functions of fluid k in the i th direction, $f_i^k(\mathbf{x}, t)$, stream with a lattice velocity \mathbf{e}_i to a neighboring node $x + \mathbf{e}_i \delta t$ at the next time step $t + \delta t$ after a collide procedure Ω_i^k .	$f_i^k(\mathbf{x} + \mathbf{e}_i \delta t, t + \delta t) = f_i^k(\mathbf{x}, t) + \Omega_i^k$ (The governing equation) (1)
Particle collision scheme	The collision operator	$\Omega_i^k = (\Omega_i^k)^3 \left[(\Omega_i^k)^1 + (\Omega_i^k)^2 \right]$ (2)
Single-phase collision for equilibrium state	The BGK operator $(\Omega_i^k)^1$ for relaxing the populations toward a local equilibrium state $f_i^{k(eq)}$ (\mathbf{x}, t). The average relaxation time $\bar{\tau}$ for ensuring continuous viscosity and pressure across phase interfaces [68].	$(\Omega_i^k)^1 = -\frac{1}{\bar{\tau}} \left[f_i^k(\mathbf{x}, t) - f_i^{k(eq)}(\mathbf{x}, t) \right]$ (3)
	The lattice velocity \mathbf{e}_i [67]	$f_i^{k(eq)}(\mathbf{x}, t) = w_i \rho_k(\mathbf{x}, t) \left[1 + 3\mathbf{e}_i \cdot \mathbf{u} + \frac{9(\mathbf{e}_i \cdot \mathbf{u})^2}{2} - \frac{3 \mathbf{u} ^2}{2} \right]$ (4)
	The lattice velocity \mathbf{e}_i [67]	$\begin{aligned} & (0, 0, 0), i = 0 \\ & (\pm 1, 0, 0), (0, \pm 1, 0), (0, 0, \pm 1), \\ & i = 1, 2, 3, 4, 5, 6 \\ & (\pm 1, \pm 1, 0), (\pm 1, 0, \pm 1), (0, \pm 1, \pm 1), \\ & i = 7, 8, 9, \dots, 18 \end{aligned}$ (5)
	Weighting coefficient w_i in D3Q19 model	$w_0 = 1/3, w_{1-6} = 1/18, w_{7-18} = 1/36$ (6)
Multiphase collision for phase separation	The perturbation operator $(\Omega_i^k)^2$ for introducing interface perturbation via color-gradient force \mathbf{F}_{kl} across the interface [66]	$(\Omega_i^k)^2 = \sum_{l \neq k} \frac{A_{kl}}{2} \mathbf{F}_{kl} \left[w_l \frac{(\mathbf{F}_{kl} \cdot \mathbf{e}_i)^2}{ \mathbf{F}_{kl} ^2} - B_i \right]$ (7)
		$\mathbf{F}_{kl} = \frac{\rho_l}{\rho} \nabla \left(\frac{\rho_k}{\rho} \right) - \frac{\rho_k}{\rho} \nabla \left(\frac{\rho_l}{\rho} \right)$ (8)
	The interfacial tension σ_{kl}	$\sigma_{kl} = \frac{\bar{\tau}}{9} (A_{kl} + A_{lk}), A_{kl} = A_{lk}$ (9)
	Parameter B_i for recovering mass and momentum conservation in D3Q19 model [70].	$B_0 = -1/3, B_{1-6} = 1/18, B_{7-18} = 1/36$ (10)
	The recoloring operator $(\Omega_i^k)^3$ for a reasonable interface and the conversation laws of density and momentum.	$(\Omega_i^k)^3 = \frac{\rho_k}{\rho} \sum_k f_i^k + \sum_{l \neq k} \beta_{kl} \frac{\rho_k \rho_l}{\rho^2} \cos(\varphi_i^{kl}) f_i^{k(eq)}$ (11)
	The angle φ_i^{kl} between \mathbf{F}_{kl} and \mathbf{e}_i	$\cos \varphi_i^{kl} = \frac{\mathbf{e}_i \cdot \mathbf{F}_{kl}(\mathbf{x}, t)}{\ \mathbf{e}_i\ \ \mathbf{F}_{kl}(\mathbf{x}, t)\ }$ (12)
	The segregation parameter β_{kl} for controlling a reasonable interfacial thickness	$\beta_{kl} = \beta_{lk} = 0.7$ (13)
Solution for macroscopic quantities	Density ρ derived from the first and moment integration of f_i^k	$\rho_k = \sum_i f_i^k = \sum_i f_i^{k(eq)}$ (14)
		$\rho = \sum_k \rho_k = \sum_i \sum_k f_i^k$ (15)
	Velocity \mathbf{u} derived from the second moment integration of f_i^k	$\rho \mathbf{u} = \sum_i \sum_k f_i^k \mathbf{e}_i$ (16)
The relationship between the relaxation time of k phase τ_k and the kinematic viscosity ν_k	c_s is lattice sound speed where the value is $\sqrt{3}/3$	$\nu_k = c_s^2 \left(\tau_k - \frac{1}{2} \right)$ (17)
The average viscosity $\bar{\nu}$		$\bar{\nu} = \rho / \sum_k \frac{\rho_k}{\nu_k}$ (18)

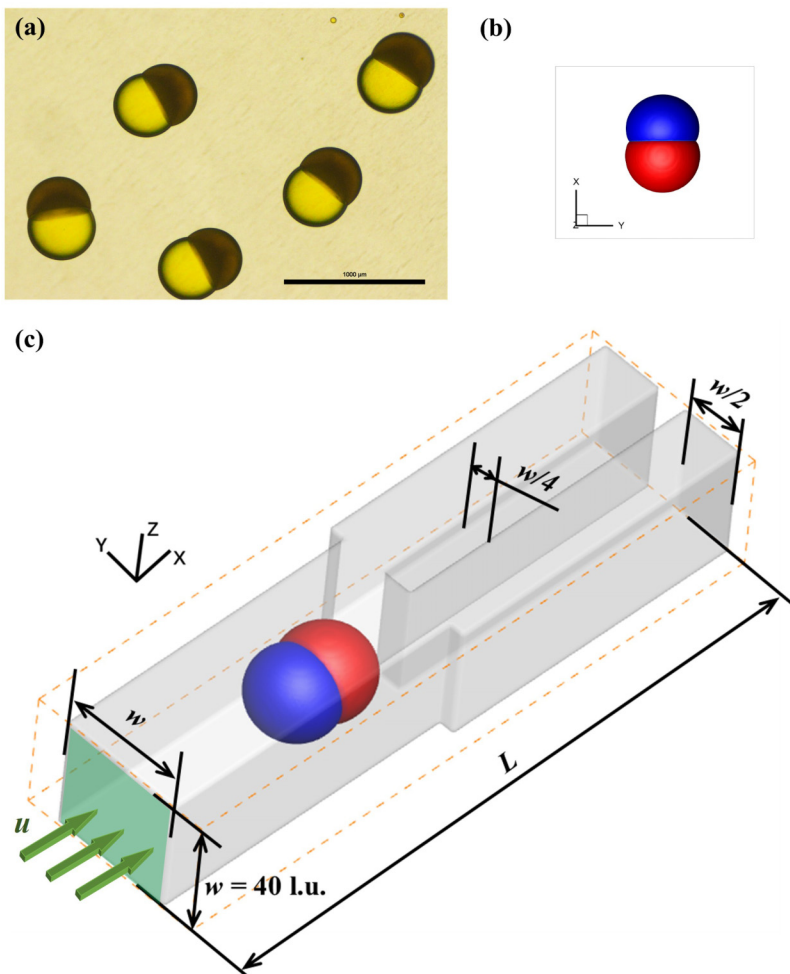


FIG. 2. (a) Experimental micrographs of the mother [bmim]FeCl₄-water Janus droplets in the bulk phase of soybean oil. Scale bar is 1000 μm. (b) The corresponding numerical result. (c) Schematic of the three-dimensional simulation domain for the breakup of Janus droplets. A uniform flow rate u is set at the channel inlet.

to the principal plane in the microscope view. The z axis represents the channel depth, and the y - z plane displays the information of the channel cross section. The characteristic parameter of the channel, w , is 40 l.u., and the cross-section area of the subchannels is half that of the main channel. The Zou-He velocity boundary scheme is applied at the inlet of the main channel, and on the two outlets, the constant-pressure Zou-He velocity boundary scheme is employed [71]. The channel walls are assumed to be fully wetted by the continuous fluid, where the no-slip midway bounce-back boundary is imposed [72,73]. The fluid domain is initialized by the continuous phase with an inlet velocity $u = 0.003$ l.u./t.s. After it reaches convergence, two droplets of the dispersed phases with equal droplet diameter D are adjacently located at the central axis of the main channel near the inlet. Varying $D \in \{16\ 20\ 24\ 26\ 28\ 30\ 32\ 36\}$, the dynamic breakup of Janus droplets in this microchannel is numerically investigated. The average capillary number of the continuous phase (Ca_{av}) is defined to show the interplay between interfacial force and viscous stress in the flows of Janus droplets as $Ca_{av} = \mu_c u_c / \sigma_{av}$, where σ_{av} is the average interfacial tension of $\sigma_{\text{water-c}}$ and $\sigma_{[\text{bmim}]\text{FeCl}_4\text{-c}}$ [40].

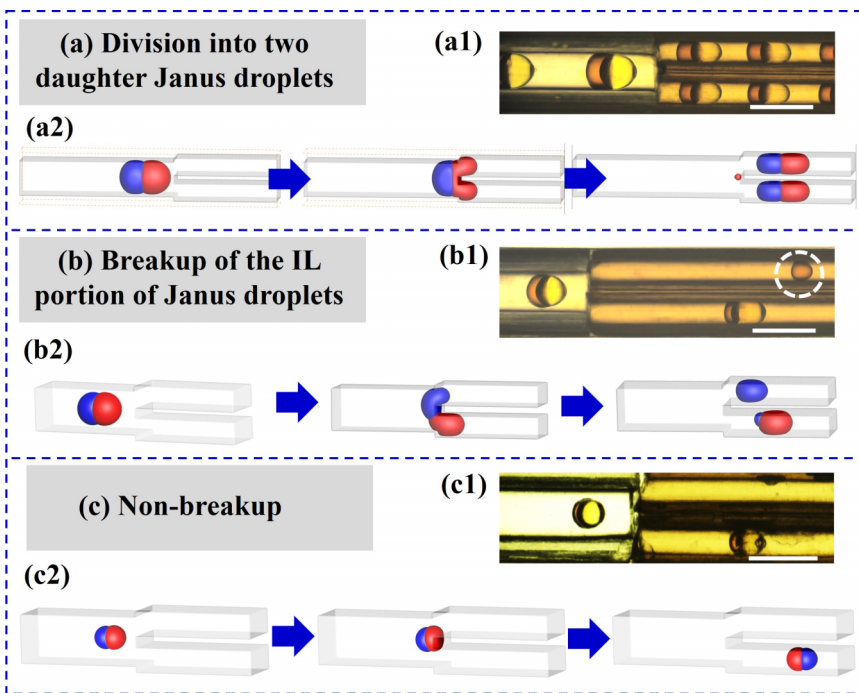


FIG. 3. Three characteristic behaviors of Janus droplets passing through the bifurcating microchannel: (a) division into two daughter Janus droplets, (b) breakup into a single-phase droplet and a smaller Janus droplet, and (c) nonbreakup. Scale bar is $1000\ \mu\text{m}$. Experimental micrographs are shown in (a1)–(c1), and corresponding simulation results are depicted in (a2)–(c2).

IV. RESULTS AND DISCUSSION

A. Flow behavior of Janus droplets in microchannel

It is known that droplet breakup at a bifurcation is attributed to the interplay of pressure drop, viscous force, and the interfacial tension [19,23,25,36,39]. From the macroscopic view, three main factors, i.e., channel geometries, physical properties of fluids (viscosity, interfacial tension), and the initial flow conditions (flow velocity, droplet size), influence the breakup of droplets [19,36]. As shown in Figs. 3(a1)–3(c1), before the mother droplets touch the segmentation obstacle, Janus droplets flow in such a way that the water semidroplet is at the front of the IL droplet in the flow direction. Therefore, an offset of centers of the two droplet pairs is observed from the top view (the x - y plane), and we found that this offset is diminished as the size of the Janus droplet decreases [see Figs. 3(a1)–3(c1)]. The flow pattern of Janus droplets in the main channel would affect the contact between Janus droplets and the obstacle, and it might also have an impact on the droplet breakup. Hence, the main contributing reasons for this flow behavior of [bmim]FeCl₄-water Janus droplets should be considered. In the flows of double emulsion droplets in microchannels, it is also observed that the core and shell droplets are not concentric [37,74]. Vian *et al.* [74] believed that the center offset of inner and outer drops of a double emulsion droplet mainly results from the pressure gradient around droplets. As a droplet flows in a constricted microchannel showing laminar flow behaviors, the pressure at the front of the droplet is lower than that at the rear [75]. It causes fluids to flow inside Janus droplets under a pressure drop Δp . The flow flux q_k of the dispersed phase k could be presented as $q_k = \frac{\Delta p}{\Delta R_k}$, where ΔR_k is the hydrodynamic resistance of the k phase. As reported by Sajeesh *et al.* [75], based on a large set of experimental data, hydrodynamic resistance induced by a single droplet flowing in a microchannel with a hydraulic radius r_h is expressed as

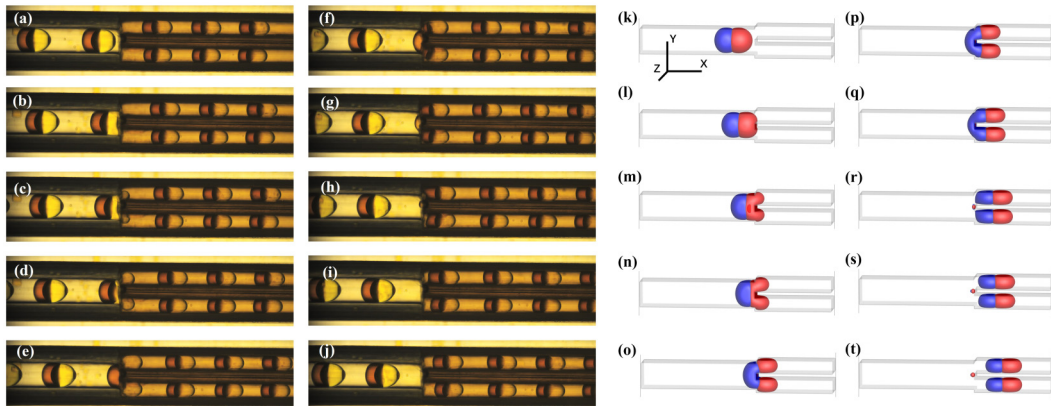


FIG. 4. Dynamic breakup of a Janus droplet that entirely plugs the main channel. [(a)–(j)] Optical micrographs of the breakup process of Janus droplets. $Q_c = 45 \mu\text{L}/\text{min}$, $Q_{\text{IL}} = Q_w = 30 \mu\text{L}/\text{min}$, where subscripts c, IL, and w represent the continuous, IL, and water phases, respectively. The interval between the successive images is 23 ms. [(k)–(t)] The corresponding results from the LB simulations with $D = 361$ u. and the initial flow rate $u = 0.0031$ u./t.s.

follows:

$$\frac{\Delta R_k}{R} = 0.01439 \lambda_k^{0.2158} \varphi_k^{3.589} - 0.001259, \quad (19)$$

where R is the hydrodynamic resistance provided by the continuous phase, λ_k denotes the viscosity ratio of the dispersed phase k to the continuous phase, and φ_k represents the size ratio of the k -phase droplet radius to r_h . In this study, the sizes of the two droplet pairs generated to form Janus droplets are the same. The viscosity of [bmim]FeCl₄ is larger than that of the water phase, as given in Table I. Thus, as a Janus droplet flows in the microchannel, the hydrodynamic resistance of the IL droplet is higher than that of the water droplet, which results in the faster flow of the water droplet than the IL phase part of a Janus droplet as shown in Figs. 3(a1) and 3(b1). As the dispersed droplet size decreases, an experimental study has shown that the hydrodynamic resistance introduced by tiny droplets can be ignored when φ_k is below 0.6 [75]. Therefore, it can be seen from Fig. 3(c1) that the centers of two droplet pairs of Janus droplets in smaller sizes are very close.

B. Dynamic breakup of IL-aqueous Janus droplets

Three characteristic flow modes of [bmim]FeCl₄-water Janus droplets passing through the bifurcated microchannel are observed: (i) division of one Janus droplet into two daughter Janus droplets [Fig. 3(a)], (ii) breakup into a single-phase droplet and a smaller Janus droplet [Fig. 3(b)], and (iii) nonbreakup [Fig. 3(c)]. The breakup regimes then would be thoroughly discussed, and 3D LB simulations are carried out to interpret the experimental observations.

1. Breakup into two daughter Janus droplets

For the case when the equivalent diameter D_e of a Janus droplet is much larger than the hydraulic diameter of the main channel, D_h , experimental observations on the breakup process and the corresponding simulation results are shown in Fig. 4. In this case, Janus droplets completely obstruct the main channel, which impedes the continuous flow. According to the pseudocolor maps of pressure distribution displayed in Fig. 5, the upstream pressure of the microchannel is obviously larger than the downstream. Driven by the pressure drop, the Janus droplet flows as a plug toward the subchannels. The front of the Janus droplet, i.e., the water drop, approaches the segmentation

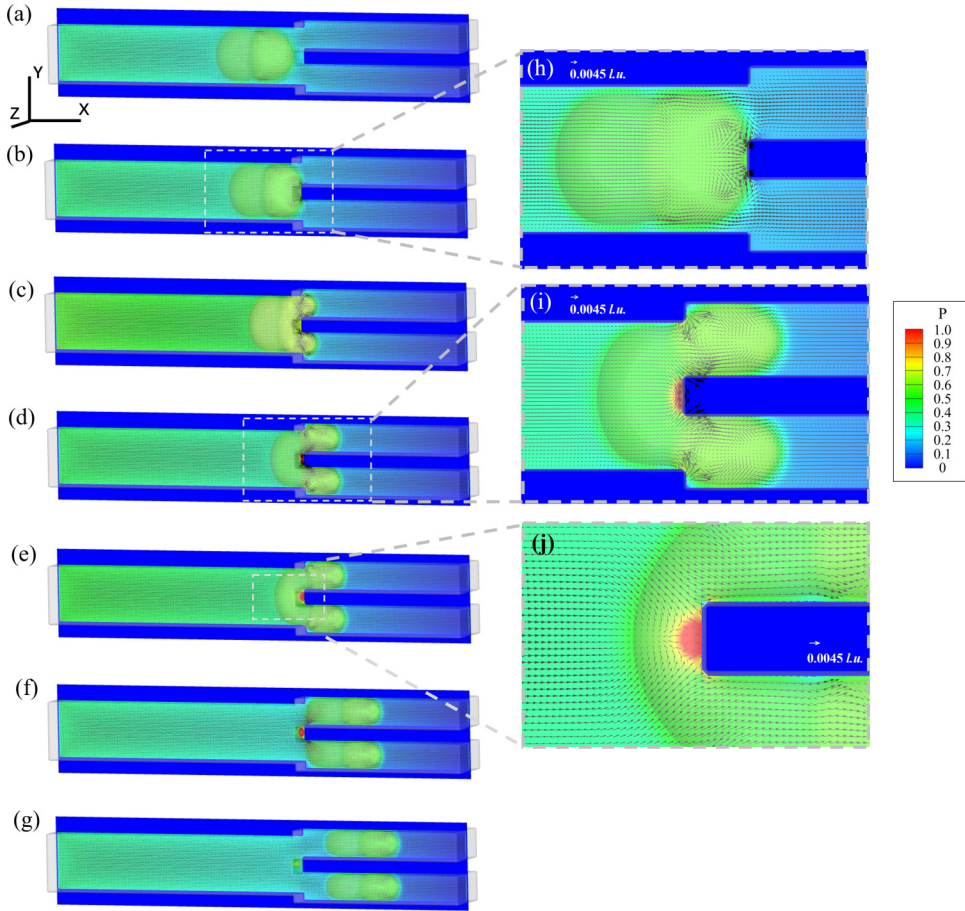


FIG. 5. The velocity vector profiles and pseudocolor maps of pressure distribution at the horizontal midplane of the microchannel during the breakup of a Janus droplet “plug” in the microchannel. [(h)–(j)] Magnified views of dashed boxes shown in (b), (d), and (e), respectively. $D = 36$ l.u., $u = 0.003$ l.u./t.s.

obstacle and deforms as presented in Figs. 4(a), 4(b), 4(k), and 4(l). Subsequently, the high pressure upstream forces the water drop passing through constrictions connecting the main channel and subchannels to divide into two identical tips in daughter channels [Figs. 4(c) and 4(m)]. As pointed out by Abate and Weitz [36], the constriction in front of the bifurcated channels enhances the constraint effect of the channel on droplets, which is good for the symmetry division of droplets. As the tips enter the subchannels, the pressure upstream further increases [Fig. 5(c)], and it propels the two tips into the subchannels [Figs. 4(d)–4(g) and 4(n)–4(q)]. The pressure inside the Janus droplet also rises due to the generation of two smaller curved surfaces until each subchannel is entirely filled, as shown in Figs. 5(c) and 5(d). The Janus droplet presented a U-shaped deformation under the geometrical constraint, where the interface of the entire Janus droplet is gradually increased due to the growth of the tips. And, vortex flows are formed inside the two tips as shown in Figs. 5(c)–5(e) and 5(i). Once the IL portion remaining in the main channel is sufficiently reduced, the thread at the front of the obstacle suddenly pinches off, resulting in two equal daughter Janus droplets [Figs. 4(h)–4(j) and 4(r)–4(t)]. Figure 5(j) reveals that the velocity vector field at the rear of the Janus droplet tends to contract inward before the breakup. And, as displayed in Figs. 5(d)–5(f), 5(i), and 5(j), the high-pressure zone is located at the front of the bifurcation, where the neck of the Janus droplet breaks up.

As shown in Fig. 4, the simulation results are quite close to the experiments, except for the behavior of the satellite droplet generated by the breakup of Janus droplets [Figs. 4(h)–4(j) and 4(r)–4(t)]. Researchers believed that a high capillary number (Ca) would lead to the formation of satellite droplets when droplets break up [23,36,76]. In the simulations, the satellite droplet stays at the front of the bifurcation [Figs. 4(r)–4(t)], whereas in the experiments, satellite droplets quickly shift to the upper branches and coalesce with daughter Janus droplets [Figs. 4(h)–4(i)], which results in a slight difference in the sizes of daughter Janus droplets between two daughter channels. It might be explained by the disturbance originated from downstream in real flow systems and the asymmetry of the channel geometry caused by the limitation of manufacture method. In an experimental study of the breakup of double emulsions, as reported by Chen *et al.* [23], when the neck remaining in the main channel gets thin enough, the capillary instability would not occur precisely at the center of the main channel accompanied with the flow perturbation in subchannels. Thus, the final breakup of the droplet is not exactly symmetrical. In LB simulations, the hydrodynamic resistance in each subchannel is identical, and the disturbance induced by the flow of daughter droplets through and out of the subchannels does not exist. Therefore, the satellite droplet stands at the center of the front of the bifurcation in numerical cases, and the daughter Janus droplets in two subchannels have the same size and shape in the simulation results.

To quantitatively investigate the breakup behaviors of the Janus droplet that completely blocks the main channel, the neck length of the mother droplet that remained in the main channel S is measured during a complete breakup process, as shown in Fig. 6. The water and IL portions of Janus droplets keep sticking together during the droplet breakup. And, since Janus droplets fully plug the main channel, the remaining portion composed of water and IL droplet can be treated as an integral one when the neck length S is measured. As illustrated by Fig. 6(q), the dimensionless neck thickness S^* linearly decreases as time goes on then undergoes a sudden decline to zero. It indicates that the regime of Janus droplet breakup with permanent obstruction consists of two stages: the squeezing stage that shows the time-linear decrease as two tips grow in the subchannels and the pinch-off stage of the neck. Figure 6(r) further confirms that the correlation between the neck length and breakup time is linear in the squeezing stage. And the droplet breakup with a larger flow rate experiences a little faster squeezing stage.

Both the qualitative and quantitative results indicate that the breakup regime of the Janus droplet, which fully plugs the main channel, is similar to the regime of breakup with permanent obstruction observed in the geometrically mediated breakup of single-phase and double emulsion droplets [23,36]. The pressure drop accumulated by the blocked continuous flow is the primary driving force for the deformation and division of Janus droplets in the bifurcating microchannel. And the final pinch off of the IL-phase neck exhibits the feature of the Rayleigh-Plateau instability [23,36].

It is worth noting that the constraint effect of the main channel on mother Janus droplets is highly important for the symmetrical breakup of Janus droplets. When the equivalent diameter of the Janus droplet, D_e , is comparable to the hydraulic diameter of the main channel, D_h , although the mother Janus droplet still breaks up into two daughter Janus droplets, the size difference of the daughter droplets between the two subchannels might be obvious [Figs. 7(a)–7(l)]. As the constraint effect of the main channel is reduced, the unstable nature of the Janus droplet flow at the junction exhibits. It can be seen from Fig. 7(b) that the central axis of the Janus droplet projecting on the x - y plane deviates from the central axis of the microchannel as the Janus droplet interacts with the front of the bifurcating obstacle. This indicates that the sizes of daughter droplets in two branches are sensitive to the placement symmetry of the Janus droplet at the junction. However, by increasing the flow rate of the continuous phase, simulation results in Figs. 7(m)–7(r) show that the mother Janus droplet with the same size as the droplet in Figs. 7(g)–7(l) could symmetrically deform at the bifurcation and split into two daughter droplets with similar sizes.

To understand the difference in droplet breakup behaviors between the two cases, Fig. 8 provides the velocity vector and pressure fields within the central x - y plane and the cross-section plane at the junction when Janus droplets reach the front of the bifurcation and divide into two tips under the two different flow rates. A comparison of Figs. 8(a) and 8(c) confirms that the larger flow rate of

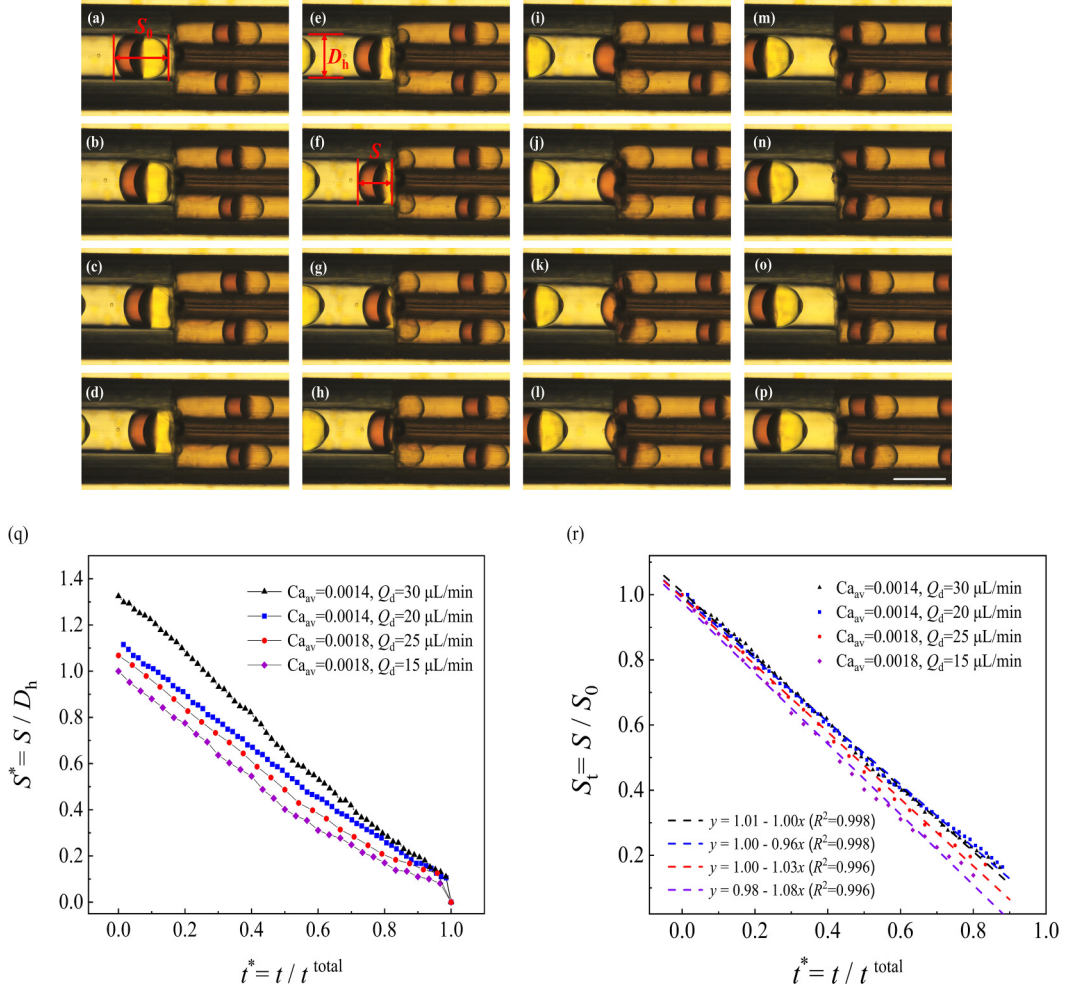


FIG. 6. The dynamic breakup of Janus droplets quantified by the evolution of the dimensionless length of mother droplets. [(a)–(p)] Magnified image sequences of a Janus droplet, which fully plugs the main channel and splits into two daughter Janus droplets. The interval between the successive images is 16 ms. $Q_c = 45 \mu\text{L}/\text{min}$, $Q_{IL} = Q_w = 30 \mu\text{L}/\text{min}$, where subscripts c, IL, and w represent the continuous, IL, and water phases, respectively. S_0 is the initial length of the mother Janus droplets along their central axes, and S is the neck length which is measured from the back interface of the Janus droplet to the front of the bifurcating obstacle. Scale bar is $1000 \mu\text{m}$. (q) The evolution of the dimensionless neck length $S^* = S/D_h$ during the breakup of a Janus droplet plug. (r) The neck length S scaled by the initial droplet length S_0 as a function of dimensionless time $t^* = t/t^{\text{total}}$ where t^{total} is the time period of a complete breakup process of a Janus droplet. $Q_d = Q_{IL} = Q_w$, where the subscript d denotes the dispersed phase.

the continuous phase provides higher pressure and viscous forces driving the droplet downstream. Under the lower flow rate, the tips of the Janus droplet extruded into the two branches are in different sizes, and the velocity vectors within the cross-section plane are denser in the lower branch than that in the upper branch, as shown in Figs. 8(b) and 8(ii). However, a symmetric flow field of the two subchannels along the central axis is generated under the higher flow rate, as displayed in Figs. 8(c), 8(d), and 8(iii), and 8(iv). The results imply that the increase in the flow rate might stabilize the symmetrical location and deformation of Janus droplets at the junction by providing large pressure drop and viscous stress.

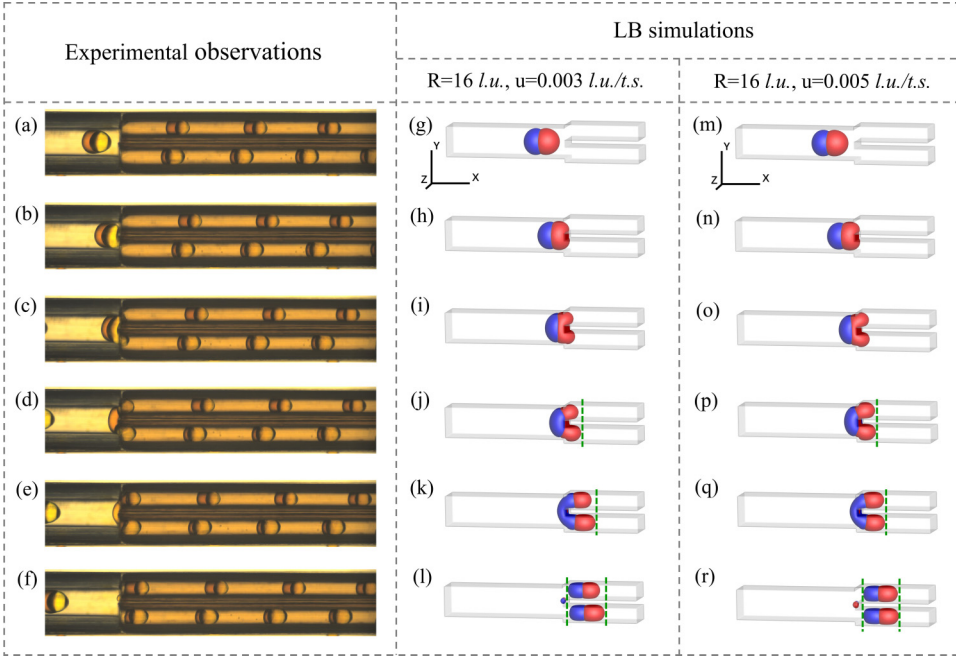


FIG. 7. Janus droplet breakup into two daughter Janus droplets with different sizes. [(a)–(f)] Optical micrographs of the breakup of Janus droplets with $Q_c = 60 \mu\text{L}/\text{min}$, $Q_{\text{IL}} = Q_w = 15 \mu\text{L}/\text{min}$, where subscripts c, IL, and w represent the continuous, IL and water phases, respectively. The simulation results [(g)–(l)] with $D = 32 \text{ l.u.}$, $u = 0.003 \text{ l.u./t.s.}$, and [(m)–(r)] with $D = 32 \text{ l.u.}$ under $u = 0.005 \text{ l.u./t.s.}$ The dashed lines which are depicted in dark green and parallel to the y axis in (j) and (k) and (p) and (q) indicate the position of the longer one of two tips of Janus droplets developed in the branches, and the dashed line in (l)–(r) denotes the extreme front and back positions of the two daughter Janus droplets occupying in the subchannels.

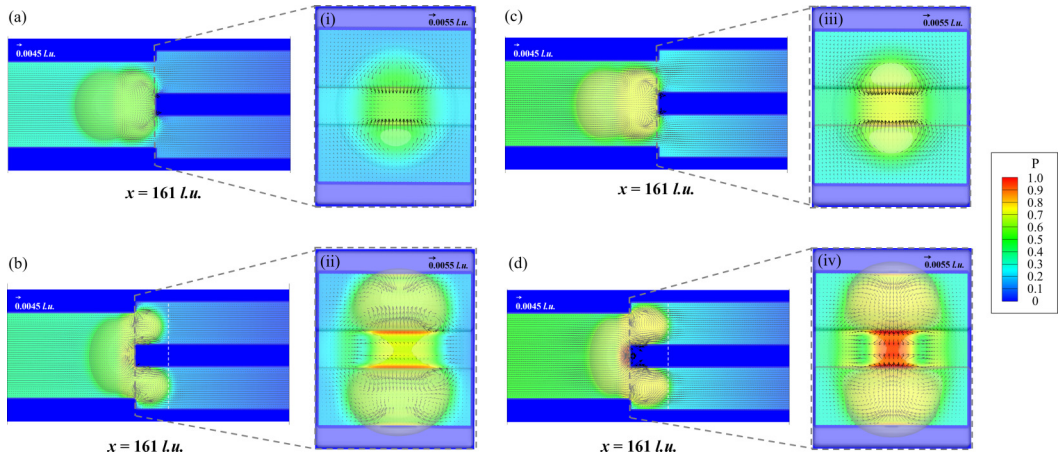


FIG. 8. The velocity vector profiles and pseudocolor maps of pressure distribution at [(a)–(d)] the horizontal midplane and [(i)–(iv)] the corresponding cross-section plane before the bifurcation ($x = 161 \text{ l.u.}$) viewed from downstream when the Janus droplet reaches the front of the bifurcating obstacle and divides into two tips under different inlet velocities u . (a), (b) $u = 0.003 \text{ l.u./t.s.}$, and (c), (d) $u = 0.005 \text{ l.u./t.s.}$

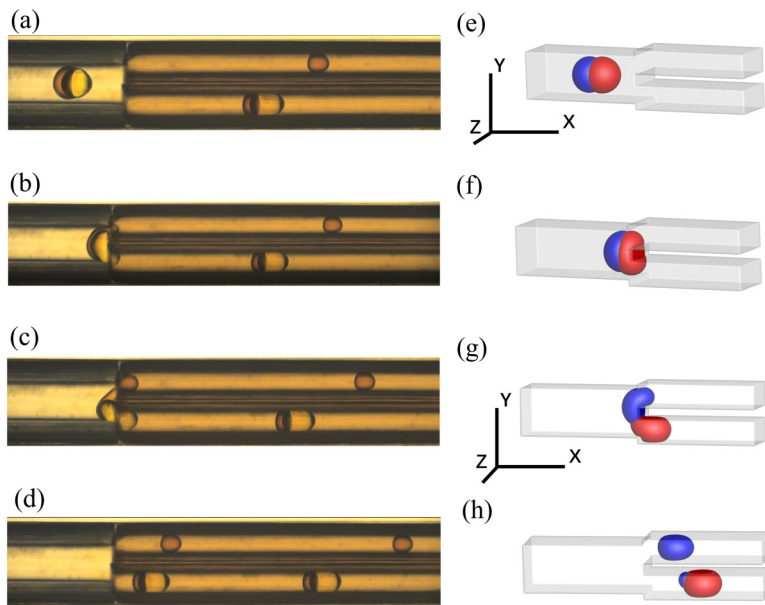


FIG. 9. Janus droplet breakup into a single-phase IL droplet and a smaller Janus droplet. [(a)–(d)] Optical micrographs of the breakup process of Janus droplets with $Q_c = 60 \mu\text{L}/\text{min}$, $Q_{\text{IL}} = Q_w = 5 \mu\text{L}/\text{min}$, where subscripts c, IL, and w represent the continuous, IL, and water phases, respectively. [(e)–(h)] The simulation results correspond to (a)–(d), with $D = 26 \text{ l.u.}$, $u = 0.003 \text{ l.u.}/\text{t.s.}$

2. Breakup into a single-phase droplet and a smaller Janus droplet

When the size of Janus droplets is below that of the main channel and D_e is commonly larger than $1/2D_h$, the breakup of the Janus droplet into a single-phase droplet and a smaller daughter Janus droplet, as shown in Fig. 9, is frequently observed. The tiny tunnel that allows the continuous phase flow exists between the droplet and the wall of the main channel. It is noted that this breakup mode of Janus droplets with tunnels is not the same as the regime of breakup with tunnels in the study of single-phase droplet breakup [15]. Tunnels in the breakup regime of single-phase droplets particularly refer to a pathway between the droplet and the daughter channels (not the main channel). The decreased constraint effect of the main channel on the mother Janus droplets and a moderate flow rate seem to favor the breakup of the IL single-phase segment.

LB simulation results shown in Figs. 9(e)–9(h) and Fig. 10 could help to explain the observation on the breakup of the IL droplet portion. As the tunnel between droplets and the wall of the main channel allows the lateral shift of the mother droplet, the Janus droplet approaches the front of the bifurcating obstacle and asymmetrically deforms. It can be seen from Figs. 9(b), 9(f), and 10(b) that the central axis of the Janus droplet slightly deviates from that of the bifurcation on the x - y projection plane. Then, the water portion of the Janus droplet enters the lower subchannel, as displayed by Figs. 9(b), 9(c), 9(f), and 9(g). While the tail of the Janus droplet is not fast enough to follow the same path as the head, the tip of the IL droplet squeezes into the upper branch due to the pressure drop and geometrical constraint [Figs. 9(c), 9(g), and 10(c)]. The IL phase portion is stretched and finally pinched off at the tip of the segmentation obstacle [Figs. 9(c), 9(d), 9(g), and 9(h)]. Figure 10(ii) shows that the high-pressure regions are located near the upper and lower tips of the front of the obstacle during the droplet deformation process. In addition, the high-pressure area at the upper tip of the obstacle is obviously larger than the lower position near the water droplet portion, as displayed in Fig. 10(iii), indicating the location of droplet breakup. It should be pointed out that the flow behavior of the breakup of the IL portion of Janus droplets is different from that of the

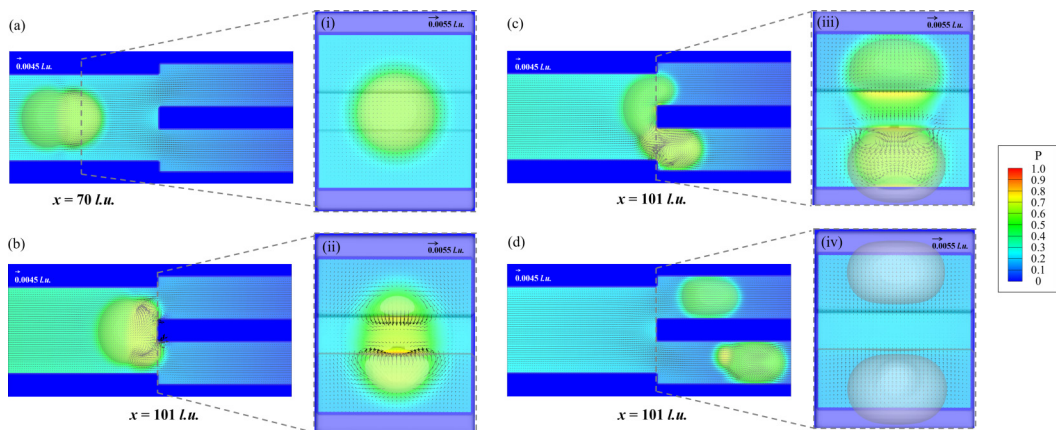


FIG. 10. The velocity vector profiles and pseudocolor maps of pressure distribution at [(a)–(d)] the horizontal midplane and [(i)–(iv)] the cross-section plane corresponding to the location of grey dashed lines in (a)–(d) during Janus droplet breakup into a single-phase IL droplet and a daughter Janus droplet. $D = 26$ l.u., $u = 0.003$ l.u./t.s.

stripping of the shell phase of double emulsions reported by Akamatsu *et al.* [37]. The shell phase of the double emulsions penetrates two subchannels during the stripping process [37], whereas the IL component of the Janus droplet enters just one of the subchannels in the majority of cases. But it can be found that the common feature between the double emulsions and Janus droplet breakup in the regime of the breakup of single-phase portions is the deviated central axis of the mother droplet from that of the bifurcation due to the unstable lateral migration of droplets at the junction.

We also found that the path of single-phase IL droplets is not always toward one specific subchannel, presenting an unstable nature. Akamatsu *et al.* [68] reported that the stripping of the shell phase of double emulsions occurs at a frequency up to 40% at a flow rate ranging from 0.5×10^{-2} to 5.0×10^{-2} m/s. It indicated that the breakup of the single-phase portion of double droplets presents randomness to some extent. Figure 11 shows the breakup modes of Janus droplets with equivalent diameters D_e approximately ranging from $0.5D_h$ to D_h under different Ca_{av} values. It can be seen from Fig. 11 that large droplet size and Ca_{av} are preferable for the Janus droplet breakup into two daughter Janus droplets. The dashed line described by $D_e/D_h = 0.95Ca_{av}^{-0.31}$ indicates that the transition from the regime of breakup of the IL single-phase portion to the regime of division into two daughter Janus droplets occurs as the increase of the normalized droplet equivalent diameter and the Ca_{av} value. In the transition mode, the two breakup regimes would both be observed: not all the droplets break up into two Janus daughter droplets; instead, some of the droplets would experience the asymmetrical breakup of the ionic liquid portion of the Janus droplets under one set of operating conditions.

3. Nonbreakup

When the equivalent droplet diameters D_e are decreased below $1/2D_h$, Janus droplets rotate after contacting the front of the obstacle, and alternately enter the upper and lower subchannels without breakup, as shown in Fig. 12. Owing to the decrease of the droplet size, the blockage of continuous flow by the droplet is reduced, and thus the upstream pressure in the microchannel [Figs. 12(k)–12(o)] is lower than that in the cases with larger Janus droplets. And the upstream pressure change induced by the flow and breakup of small droplets is less intense. Figures 12(k)–12(o) also demonstrate that the Laplace pressure inside two smaller droplet pairs is much larger than that in the bigger one (see Figs. 5, 8, and 10). In the nonbreakup regime, the interfacial tensions of the droplet would overcome the combined effect of the pressure drop, the shear force, and the

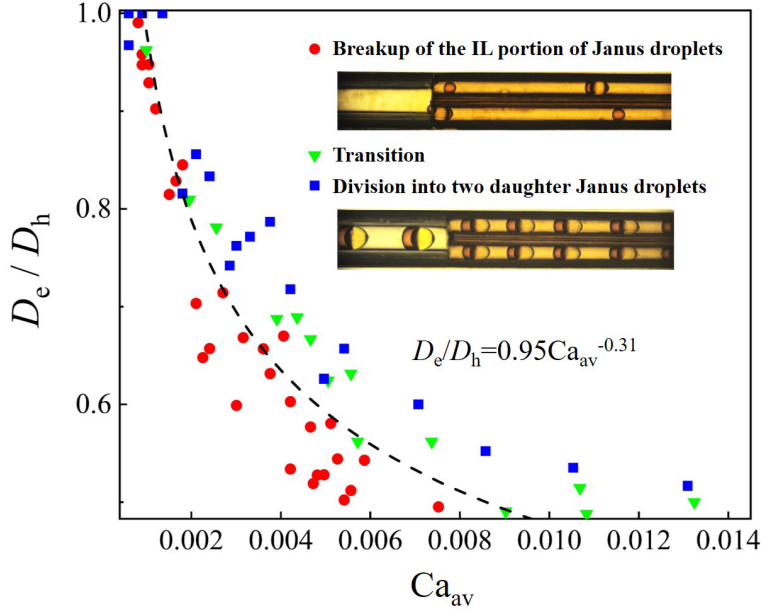


FIG. 11. The diagram of the breakup behaviors of Janus droplets with the ratio of the droplet equivalent diameter D_e to the hydraulic diameter of the main channel, D_h , ranging from 0.5 to 1 under different Ca_{av} values. The dashed line is given by $\frac{D_e}{D_h} = 0.95Ca_{av}^{-0.31}$ and indicates that droplet breakup into two daughter Janus droplets gradually occurs as the increase of the initial droplet size and the Ca_{av} value. The green inverted triangle denotes the transition mode, where the two breakup regimes would both be observed at varying frequencies of occurrence.

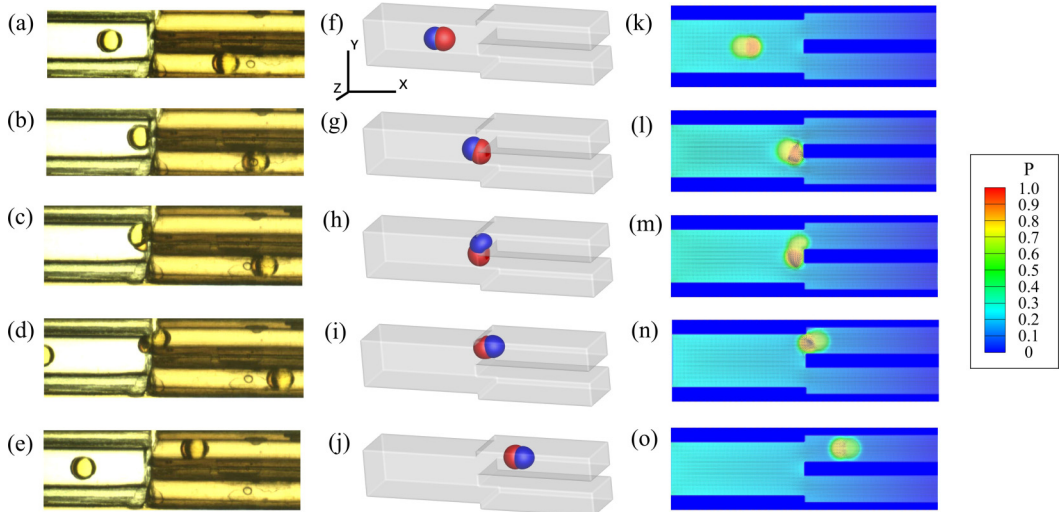


FIG. 12. The behaviors of Janus droplets for the nonbreakup regime. [(a)–(e)] Optical micrographs of Janus droplets shifting to one of the subchannels without breakup. $Q_c = 60 \mu\text{L}/\text{min}$, $Q_{IL} = Q_w = 5 \mu\text{L}/\text{min}$, where subscripts c, IL, and w represent the continuous, IL, and water phases, respectively. [(f)–(j)] The simulation results corresponding to (a)–(e), with $D = 16$ l.u., $u = 0.003$ l.u./t.s. [(k)–(o)] The corresponding velocity vector profiles and pseudocolor maps of pressure distribution at the horizontal midplane of the microchannel.

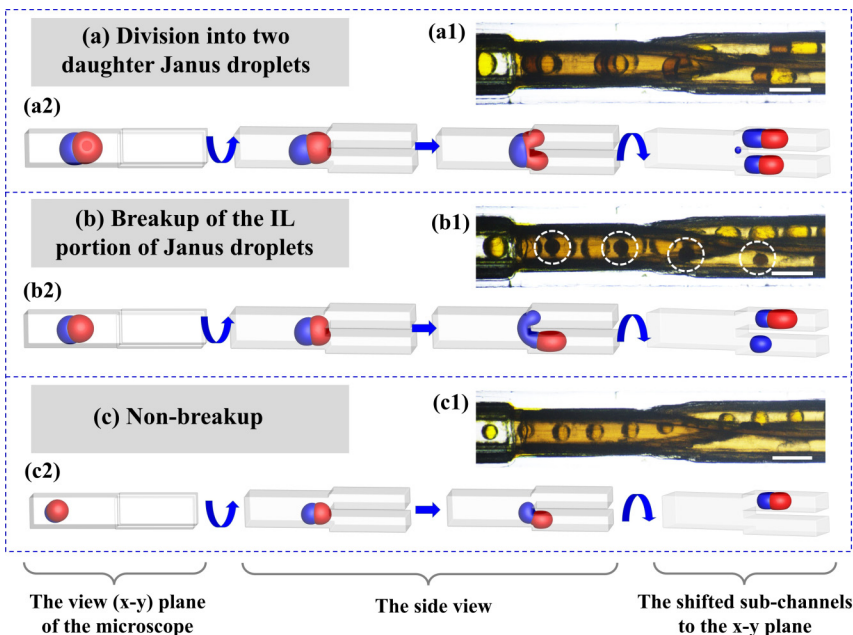


FIG. 13. Three characteristic behaviors of Janus droplets passing through the rotated splitting microchannel with the obstacle parallel to the x - y plane. The experimental micrographs of Janus droplet breakup: (a1) $Q_c = 25 \mu\text{L}/\text{min}$, $Q_{\text{IL}} = Q_w = 13 \mu\text{L}/\text{min}$. (b1) $Q_c = 20 \mu\text{L}/\text{min}$, $Q_{\text{IL}} = Q_w = 8 \mu\text{L}/\text{min}$. (c1) $Q_c = 60 \mu\text{L}/\text{min}$, $Q_{\text{IL}} = Q_w = 5 \mu\text{L}/\text{min}$. The subscripts c, IL, and w represent the continuous, IL, and water phases, respectively. Scale bar is $500 \mu\text{m}$. [(a2)–(c2)] The numerical results, corresponding to (a1)–(c1), respectively.

confined geometry, which keeps the Janus droplet intact. Increasing the flow rate of the continuous phase, the breakup of small Janus droplets might occur due to the increase of the shear stress, but it is hardly controlled, and large amounts of satellite droplets would be generated.

C. Change of the baffle orientation of the bifurcating microchannel

Experimental and numerical results in the above section indicate that the breakup of Janus droplets is influenced by the precise placement of Janus droplets at the junction, especially when the constraint effect of the main channel is reduced. Unlike the single-phase or double emulsion droplets, the dumbbell-shaped [bmim]FeCl₄-water Janus droplets exhibit oblique flow in the main channel because the water portion of the Janus droplet is upward anterior of the IL drop in the flow direction as discussed in Sec. IV A. The splitting geometry [see Figs. 1(b1) and 1(b2)] adopted in Sec. IV B might not be used to fully demonstrate the effect of the oblique flow of the Janus droplet because the obstacle is vertical to the view plane of the microscope (x - y plane). In order to give a full description of the breakup behaviors of Janus droplets under different baffle orientations, the bifurcating microchannel is rotated 90° , where the obstacle becomes parallel to the x - y plane, as shown in Figs. 1(c1) and 1(c2). In addition, the rear of the top subchannel is repositioned as the lower branch at the x - y plane, and the end of the bottom subchannel is shifted to the x - y plane as the upper branch through 3D printing manufacture, facilitating direct observation on the view plane of the microscope.

Likewise, three typical modes are observed when Janus droplets pass through the rotated splitting microchannel, as shown in Figs. 13(a1)–13(c1), and the corresponding numerical results are presented in Figs. 13(a2)–13(c2). Compared with the breakup behaviors presented in the microchannel with the perpendicular obstacle (see Sec. IV B), asymmetrical breakup of Janus droplets more

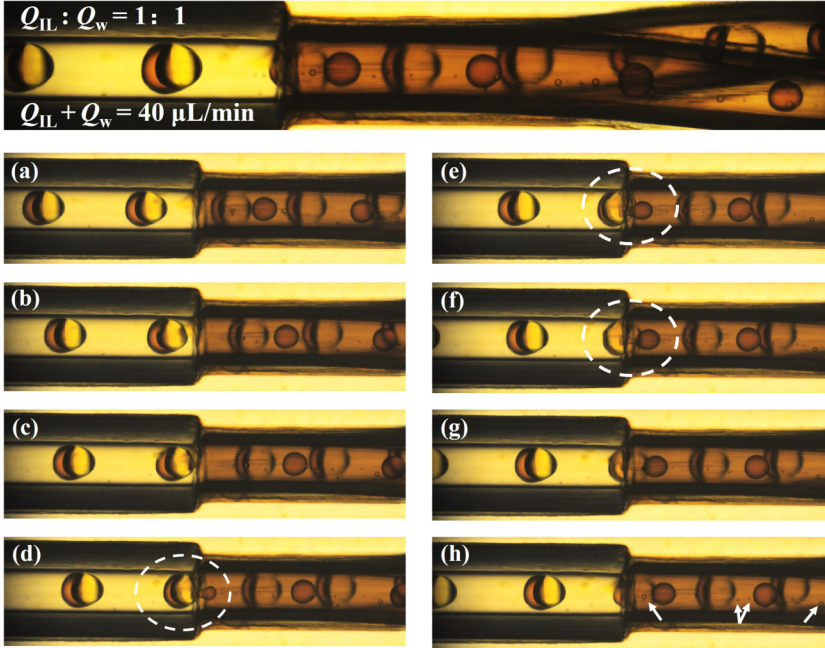


FIG. 14. Image sequences of Janus droplet breakup into a single-phase IL droplet and a smaller Janus droplet in the rotated splitting microchannel with the front bifurcating obstacle parallel to the x - y plane. The interval between (a) and (b) is 50 ms, while images (c)–(h) have a time interval of 20 ms. $Q_c = 70 \mu\text{L}/\text{min}$, $Q_{\text{IL}} = Q_w = 20 \mu\text{L}/\text{min}$, where subscripts c, IL, and w represent the continuous, IL, and water phases, respectively. The white arrows in (h) indicate the generation of the satellite droplets.

frequently occurs in the rotated splitting microchannel. This discrepancy could be explained by the simulation results in Figs. 13(a2)–13(c2). As long as sufficient space is provided for the vertical migration of Janus droplets in the main channel, Janus droplets would obliquely contact the obstacle, as demonstrated from the side view in Figs. 13(a2) and 13(b2), resulting in the asymmetrical breakup where the daughter droplets in the top subchannel are generally smaller than those in the bottom subchannel [see Figs. 13(a1) and 13(b1)] and the shifted subchannels to the x - y plane as shown in Figs. 13(a2) and 13(b2)]. This might be one of the reasons that leads to another difference in the regime of breakup of the IL single-phase portion between two baffle orientations. In the rotated splitting microchannel, even at large flow rates, the single-phase IL droplets could still be steadily stripped from Janus droplets with small sizes (see Fig. S2 in the Supplemental Material [64]). When the D_e of mother droplets is close to $0.5D_h$, Janus droplets might pass into the bottom branch without breakup as the contact position of Janus droplets with the obstacle is far below the horizontal center axis of the microchannel [see Figs. 13(c1) and 13(c2)].

Figure 14 demonstrates the dynamic breakup of the IL portion of Janus droplets in the rotated splitting microchannel. It can be seen from Figs. 14(d)–14(h) that, as the tip of the IL droplet enters the top branch, the Janus droplet containing the water drop quickly rolls after making contact with the obstacle, and ultimately passes into the bottom branch. And, as shown in Fig. 14(h), the final breakup of the IL droplet forms little satellite droplets. It should be pointed out that the single-phase IL droplets always shift to the top subchannel in the rotated splitting microchannel, whereas in the splitting microchannel with the obstacle which is perpendicular to the x - y plane, the path of the single-phase IL droplets is largely random (see Fig. 9 and the inset in Fig. 11) because of the unstable lateral location of droplets at the junction induced by flow disturbance. Figure 15 shows the map of the breakup modes of Janus droplets in the rotated splitting microchannel. In comparison with the results in Fig. 11, the transition region here moves to the upper left, and the region of

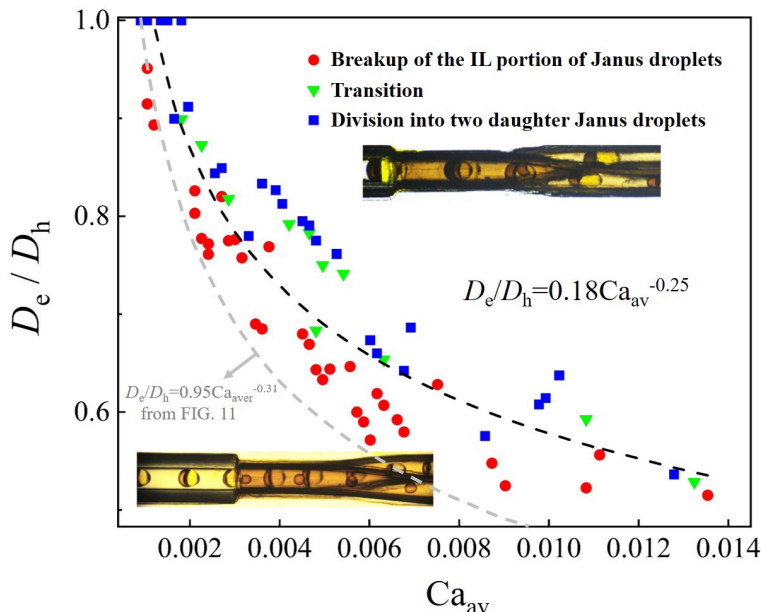


FIG. 15. The diagram of the breakup behaviors of the Janus droplets with $0.5D_h < D_e < D_h$ in the rotated splitting microchannel with the bifurcating obstacle parallel to the x - y plane under different Ca_{av} values. The dashed line is given by $D_e/D_h = 0.18Ca_{av}^{-0.25}$ and indicates that droplet breakup into two daughter Janus droplets gradually occurs as the increase of the initial droplet size and the Ca_{av} value. The gray dashed line is the fitting curve in Fig. 11, indicating the transition of the two breakup regimes in the splitting microchannel where the baffle is vertical to the x - y plane.

breakup of the IL single-phase portion in the operation map expands. It confirms that Janus droplets are more prone to asymmetrically break up in the microchannel with the baffle parallel to the x - y plane than with the erected baffle in the x - y plane.

V. CONCLUSION

In summary, we performed microfluidic experiments and three-dimensional LB simulations to investigate the dynamic breakup of ionic liquid (IL)-water Janus droplets in a bifurcating microchannel. Three different flow modes are characterized: (i) division into two daughter Janus droplets, (ii) breakup into a single-phase droplet and a smaller daughter Janus droplet, and (iii) nonbreakup. When Janus droplets fully plug the channel, they divide into two daughter Janus droplets, where the breakup regime of Janus droplets is similar to the regime of breakup with permanent obstruction reported in the studies of the geometrically mediated breakup of single-phase and double emulsion droplets [23,36]. Experimental results demonstrate that the breakup of a Janus droplet “plug” experiences two stages: the squeezing stage where the dimensionless length of the mother droplet remaining in the main channel presents a time linear decrease, and the pinch-off stage of the neck of the IL phase. As the initial droplet size decreases, the constraint effect of the main channel on mother droplets reduces, and the symmetric placement of Janus droplets at the bifurcation becomes unstable, resulting in the size difference of the daughter Janus droplets between two subchannels. It is found that the strong confined effect of the main channel and large flow rates of the continuous phase are vitally important for the symmetrical breakup of Janus droplets. The tunnel between the mother droplet and the wall of the main channel, which allows the lateral shift of the droplet, and moderate flow rates facilitate the breakup of the IL single-phase portion of Janus droplets. Compared with the experimental study by Akamatsu *et al.* [37], although the flow behavior of stripping double

emulsion of the shell phase differs from that of partially stripping the Janus droplet of the IL portion, the common feature between the breakup of the double emulsion and Janus droplets in the regime of breakup of the single-phase portion is the deviated central axis of the mother droplet from that of the bifurcation induced by the unstably lateral migration of droplets at the junction. The map of the breakup modes of Janus droplets identified the transition between the two breakup modes and confirms that large droplet size and Ca_{av} value are favorable to the regime of breakup into two daughter Janus droplets.

In particular, unlike the single-phase or double emulsion droplets, the dumbbell-shaped [bmim]FeCl₄-water Janus droplets might exhibit oblique flow in the main channel due to the different hydrodynamic resistances between two semidroplets. The water portion of the Janus droplet is upward anterior of the [bmim]FeCl₄ drop in the flow direction. It is demonstrated that Janus droplets are inclined to asymmetrically split after 90° rotation of the splitting microchannel with the obstacle parallel to the x - y plane. Results indicate that the breakup of Janus droplets is influenced by the precise placement of the droplets at the junction. Our findings elucidate parts of the physics governing the geometrically mediated breakup of Janus droplets in microchannels. Future studies could include the influence of surfactant and channel wettability to obtain a full description of the Janus droplet breakup, and the multistage breakup of Janus droplets for the high-throughput microfluidic production of Janus droplets.

ACKNOWLEDGMENT

The financial support from National Natural Science Foundation (Grant No. 21991104) is acknowledged.

-
- [1] J. Atencia and D. J. Beebe, Controlled microfluidic interfaces, *Nature (London)* **437**, 648 (2005).
 - [2] A. M. Nightingale, T. W. Phillips, J. H. Bannock, and J. C. de Mello, Controlled multistep synthesis in a three-phase droplet reactor, *Nat. Commun.* **5**, 3777 (2014).
 - [3] T. Y. Lee, T. M. Choi, T. S. Shim, R. A. M. Frijns, and S.-H. Kim, Microfluidic production of multiple emulsions and functional microcapsules, *Lab Chip* **16**, 3415 (2016).
 - [4] A. E. Goodling, S. Nagelberg, B. Kaehr, C. H. Meredith, S. I. Cheon, A. P. Saunders, M. Kolle, and L. D. Zarzar, Colouration by total internal reflection and interference at microscale concave interfaces, *Nature (London)* **566**, 523 (2019).
 - [5] I. C. Clark *et al.*, HIV silencing and cell survival signatures in infected T cell reservoirs, *Nature (London)* **614**, 318 (2023).
 - [6] B. Li, X. Chen, Y. Zhou, Y. Zhao, T. Song, X. Wu, and W. Shi, Liquid-liquid phase separation of immiscible polymers at double emulsion interfaces for configurable microcapsules, *J. Colloid Interface Sci.* **641**, 299 (2023).
 - [7] P. A. Zhu and L. Q. Wang, Passive and active droplet generation with microfluidics: A review, *Lab Chip* **17**, 34 (2017).
 - [8] L.-Y. Chu, A. S. Utada, R. K. Shah, J.-W. Kim, and D. A. Weitz, Controllable monodisperse multiple emulsions, *Angew. Chem. Int. Ed.* **46**, 8970 (2007).
 - [9] C. H. Chen, R. K. Shah, A. R. Abate, and D. A. Weitz, Janus particles templated from double emulsion droplets generated using microfluidics, *Langmuir* **25**, 4320 (2009).
 - [10] S. Nawar, J. K. Stolaroff, C. W. Ye, H. Y. Wu, D. T. Nguyen, F. Xin, and D. A. Weitz, Parallelizable microfluidic dropmakers with multilayer geometry for the generation of double emulsions, *Lab Chip* **20**, 147 (2020).
 - [11] R. Seemann, M. Brinkmann, T. Pfohl, and S. Herminghaus, Droplet based microfluidics, *Rep. Prog. Phys.* **75**, 016601 (2012).

- [12] S. Sohrabi, N. Kassir, and M. K. Moraveji, Droplet microfluidics: Fundamentals and its advanced applications, *RSC Adv.* **10**, 27560 (2020).
- [13] T. Porto Santos, C. M. Cejas, and R. L. Cunha, Microfluidics as a tool to assess and induce emulsion destabilization, *Soft Matter* **18**, 698 (2022).
- [14] D. R. Link, S. L. Anna, D. A. Weitz, and H. A. Stone, Geometrically mediated breakup of drops in microfluidic devices, *Phys. Rev. Lett.* **92**, 054503 (2004).
- [15] M. C. Jullien, M. J. Tsang Mui Ching, C. Cohen, L. Menetrier, and P. Tabeling, Droplet breakup in microfluidic T-junctions at small capillary numbers, *Phys. Fluids* **21**, 072001 (2009).
- [16] A. M. Leshansky and L. M. Pismen, Breakup of drops in a microfluidic T junction, *Phys. Fluids* **21**, 023303 (2009).
- [17] X. Sun, C. Y. Zhu, T. T. Fu, Y. G. Ma, and H. Z. Li, Dynamics of droplet breakup and formation of satellite droplets in a microfluidic T-junction, *Chem. Eng. Sci.* **188**, 158 (2018).
- [18] M. Yamada, S. Doi, H. Maenaka, M. Yasuda, and M. Seki, Hydrodynamic control of droplet division in bifurcating microchannel and its application to particle synthesis, *J. Colloid Interface Sci.* **321**, 401 (2008).
- [19] X. Wang, Z. M. Liu, and Y. Pang, Breakup dynamics of droplets in an asymmetric bifurcation by μ PIV and theoretical investigations, *Chem. Eng. Sci.* **197**, 258 (2019).
- [20] S. Protière, M. Z. Bazant, D. A. Weitz, and H. A. Stone, Droplet breakup in flow past an obstacle: A capillary instability due to permeability variations, *Europhys. Lett.* **92**, 54002 (2010).
- [21] L. Salkin, L. Courbin, and P. Panizza, Microfluidic breakups of confined droplets against a linear obstacle: The importance of the viscosity contrast, *Phys. Rev. E* **86**, 036317 (2012).
- [22] L. Salkin, A. Schmit, L. Courbin, and P. Panizza, Passive breakups of isolated drops and one-dimensional assemblies of drops in microfluidic geometries: Experiments and models, *Lab Chip* **13**, 3022 (2013).
- [23] Y. P. Chen, W. Gao, C. B. Zhang, and Y. J. Zhao, Three-dimensional splitting microfluidics, *Lab Chip* **16**, 1332 (2016).
- [24] W. Gao, C. Yu, and F. Yao, Droplets breakup via a splitting microchannel, *Chin. Phys. B* **29**, 054702 (2020).
- [25] Y. Ren, K. S. Koh, M. Yew, J. K. Chin, Y. Chan, and Y. Y. Yan, Droplet breakup dynamics in bi-layer bifurcating microchannel, *Micromachines* **9**, 57 (2018).
- [26] Z. Li, L. Li, M. Liao, L. He, and P. Wu, Multiple splitting of droplets using multi-furcating microfluidic channels, *Biomicrofluidics* **13**, 024112 (2019).
- [27] S. Wu, L. Wu, J. Chen, C. Zhang, X. Liu, Y. Chen, and W. Gao, Splitting behaviors of droplets in fractal tree-shaped microchannels, *Int. J. Multiphase Flow* **163**, 104440 (2023).
- [28] H. Chen, J. Li, H. C. Shum, H. A. Stone, and D. A. Weitz, Breakup of double emulsions in constrictions, *Soft Matter* **7**, 2345 (2011).
- [29] L. Rosenfeld, L. Fan, Y. Chen, R. Swoboda, and S. K. Y. Tang, Break-up of droplets in a concentrated emulsion flowing through a narrow constriction, *Soft Matter* **10**, 421 (2014).
- [30] C. Dai, S. Fang, Y. Wu, X. Wu, M. Zhao, C. Zou, H. Li, H. Zhou, and K. Zhang, Experimental study of bubble breakup process in non-Newtonian fluid in 3-D pore-throat microchannels, *Colloids Surf. A* **535**, 130 (2017).
- [31] A. D. Bick, J. W. Khor, Y. Gai, and S. K. Y. Tang, Strategic placement of an obstacle suppresses droplet break up in the hopper flow of a microfluidic soft crystal, *Proc. Natl. Acad. Sci. USA* **118**, e2017822118 (2021).
- [32] K. S. Jayaprakash and A. K. Sen, Continuous splitting of aqueous droplets at the interface of co-flowing immiscible oil streams in a microchannel, *Soft Matter* **14**, 725 (2018).
- [33] M. S. Abbasi, R. Song, and J. Lee, Breakups of an encapsulated surfactant-laden aqueous droplet under a DC electric field, *Soft Matter* **15**, 8905 (2019).
- [34] J. Park, J. H. Jung, K. Park, G. Destgeer, H. Ahmed, R. Ahmad, and H. J. Sung, On-demand acoustic droplet splitting and steering in a disposable microfluidic chip, *Lab Chip* **18**, 422 (2018).
- [35] Y. Wu, T. Fu, Y. Ma, and H. Z. Li, Active control of ferrofluid droplet breakup dynamics in a microfluidic T-junction, *Microfluid. Nanofluid.* **18**, 19 (2015).
- [36] A. R. Abate and D. A. Weitz, Faster multiple emulsification with drop splitting, *Lab Chip* **11**, 1911 (2011).

- [37] K. Akamatsu, K. Minezaki, M. Yamada, M. Seki, and S.-i. Nakao, Direct observation of splitting in oil-in-water-in-oil emulsion droplets via a microchannel mimicking membrane pores, *Langmuir* **33**, 14087 (2017).
- [38] M. S. Abbasi, R. Song, H. Kim, and J. Lee, Multimodal breakup of a double emulsion droplet under an electric field, *Soft Matter* **15**, 2292 (2019).
- [39] Z. Liu, D. Li, X. Wang, Y. Pang, Y. Ma, M. Li, and J. Wang, Breakup regimes of double emulsion droplets in a microfluidic Y-junction, *Phys. Fluids* **33**, 102009 (2021).
- [40] T. Nisisako and T. Torii, Formation of biphasic Janus droplets in a microfabricated channel for the synthesis of shape-controlled polymer microparticles, *Adv. Mater.* **19**, 1489 (2007).
- [41] A. Walther and A. H. Muller, Janus particles: Synthesis, self-assembly, physical properties, and applications, *Chem. Rev.* **113**, 5194 (2013).
- [42] T. Nisisako, T. Torii, T. Takahashi, and Y. Takizawa, Synthesis of monodisperse bicolored Janus particles with electrical anisotropy using a microfluidic co-flow system, *Adv. Mater.* **18**, 1152 (2006).
- [43] S. W. Han, S. E. Choi, D. H. Chang, D. Lee, B. Kim, H. Yang, M. Seo, and J. W. Kim, Colloidal pixel-based micropatterning using uniform Janus microparticles with tunable anisotropic particle geometry, *Adv. Funct. Mater.* **29**, 1805392 (2019).
- [44] B. Greydanus, D. K. Schwartz, and J. W. Medlin, Controlling catalyst-phase selectivity in complex mixtures with amphiphilic Janus particles, *ACS Appl. Mater. Interfaces* **12**, 2338 (2020).
- [45] I. U. Khan, C. A. Serra, N. Anton, X. Li, R. Akasov, N. Messaddeq, I. Kraus, and T. F. Vandamme, Microfluidic conceived drug loaded Janus particles in side-by-side capillaries device, *Int. J. Pharm.* **473**, 239 (2014).
- [46] Z. Barikbin, M. T. Rahman, P. Parthiban, A. S. Rane, V. Jain, S. Duraiswamy, S. H. Lee, and S. A. Khan, Ionic liquid-based compound droplet microfluidics for “on-drop” separations and sensing, *Lab Chip* **10**, 2458 (2010).
- [47] M. L. Li, R. Seemann, and J. B. Fleury, Active Janus droplet as a micro-reactor for automatic DNA/RNA precipitation and extraction, *ChemistrySelect* **6**, 3722 (2021).
- [48] P. S. Marques, B. D. Frank, A. Savateev, and L. Zeininger, Janus emulsion solar concentrators as photocatalytic droplet microreactors, *Adv. Opt. Mater.* **9**, 2101139 (2021).
- [49] W. Yu, Z.-L. Deng, S.-C. Wu, C. Yu, and C. Wang, Hydrodynamics of double emulsion passing through a microfluidic Y-junction, *Acta Phys. Sin.* **68**, 054701 (2019).
- [50] J. Zhou, Y.-M. Ducimetière, D. Migliozi, L. Keiser, A. Bertsch, F. Gallaire, and P. Renaud, Breaking one into three: Surface-tension-driven droplet breakup in T-junctions, *Phys. Rev. Fluids* **8**, 054201 (2023).
- [51] J. Zhang, Lattice Boltzmann method for microfluidics: Models and applications, *Microfluid. Nanofluid.* **10**, 1 (2011).
- [52] X. Q. Xing, D. L. Butler, S. H. Ng, Z. F. Wang, S. Danyluk, and C. Yang, Simulation of droplet formation and coalescence using lattice Boltzmann-based single-phase model, *J. Colloid Interface Sci.* **311**, 609 (2007).
- [53] E. van der Zwan, R. van der Sman, K. Schroen, and R. Boom, Lattice Boltzmann simulations of droplet formation during microchannel emulsification, *J. Colloid Interface Sci.* **335**, 112 (2009).
- [54] Y. Fu, L. Bai, Y. Jin, and Y. Cheng, Theoretical analysis and simulation of obstructed breakup of microdroplet in T-junction under an asymmetric pressure difference, *Phys. Fluids* **29**, 032003 (2017).
- [55] H. H. Liu, Y. Lu, S. Li, Y. Yu, and K. C. Sahu, Deformation and breakup of a compound droplet in three-dimensional oscillatory shear flow, *Int. J. Multiphase Flow* **134**, 103472 (2021).
- [56] O. Shardt, J. J. Derksen, and S. K. Mitra, Simulations of droplet coalescence in simple shear flow, *Langmuir* **29**, 6201 (2013).
- [57] W. T. Wang, T. Shao, S. F. Zhao, Y. Jin, and Y. Cheng, Experimental and numerical study of mixing behavior inside droplets in microchannels, *AIChE J.* **59**, 1801 (2013).
- [58] Y. H. Fu, L. Bai, K. H. Luo, Y. Jin, and Y. Cheng, Modeling mass transfer and reaction of dilute solutes in a ternary phase system by the lattice Boltzmann method, *Phys. Rev. E* **95**, 043304 (2017).
- [59] Y. H. Fu, L. Bai, S. F. Zhao, K. X. Bi, Y. Jin, and Y. Cheng, Droplet in droplet: LBM simulation of modulated liquid mixing, *Chem. Eng. Sci.* **155**, 428 (2016).

- [60] Y. H. Fu, S. F. Zhao, L. Bai, Y. Jin, and Y. Cheng, Numerical study of double emulsion formation in microchannels by a ternary Lattice Boltzmann method, *Chem. Eng. Sci.* **146**, 126 (2016).
- [61] Y. Fu, L. Bai, K. Bi, S. Zhao, Y. Jin, and Y. Cheng, Numerical study of Janus droplet formation in microchannels by a lattice Boltzmann method, *Chem. Eng. Process.* **119**, 34 (2017).
- [62] H. Wang, Y. Fu, Y. Wang, L. Yan, and Y. Cheng, Three-dimensional lattice Boltzmann simulation of Janus droplet formation in Y-shaped co-flowing microchannel, *Chem. Eng. Sci.* **225**, 115819 (2020).
- [63] R. Zhou, S. Li, L. Shi, N. Wang, Y. Liu, and H. Liu, Modeling and simulation of the penetration of a compound droplet into a throat in a pore-throat structure, *Phys. Fluids* **35**, 023328 (2023).
- [64] See Supplemental Material at <http://link.aps.org/supplemental/10.1103/PhysRevFluids.9.064203> for size distributions of daughter Janus droplets and optical micrographs of the IL portion breakup of Janus droplets in the rotated microchannel at different flow rates.
- [65] P. Guo, C. F. Zeng, C. Q. Wang, and L. X. Zhang, Magnetic ionic liquid-water Janus droplets: Preparation, structure and morphology adjustment and magnetic manipulation, *AIChE J.* **63**, 4115 (2017).
- [66] S. Leclaire, M. Reggio, and J.-Y. Trépanier, Progress and investigation on lattice Boltzmann modeling of multiple immiscible fluids or components with variable density and viscosity ratios, *J. Comput. Phys.* **246**, 318 (2013).
- [67] Y. H. Qian, D. Dhumieres, and P. Lallemand, Lattice BGK models for Navier-Stokes equation, *Europhys. Lett.* **17**, 479 (1992).
- [68] P. L. Bhatnagar, E. P. Gross, and M. Krook, A model for collision processes in gases. I. Small amplitude processes in charged and neutral one-component systems, *Phys. Rev.* **94**, 511 (1954).
- [69] M. Latva-Kokko and D. H. Rothman, Diffusion properties of gradient-based lattice Boltzmann models of immiscible fluids, *Phys. Rev. E* **71**, 056702 (2005).
- [70] T. Reis and T. N. Phillips, Lattice Boltzmann model for simulating immiscible two-phase flows, *J. Phys. A: Math. Gen.* **40**, 4033 (2007).
- [71] Q. S. Zou and X. Y. He, On pressure and velocity boundary conditions for the lattice Boltzmann BGK model, *Phys. Fluids* **9**, 1591 (1997).
- [72] U. Dortona, D. Salin, M. Cieplak, R. B. Rybka, and J. R. Banavar, Two-color nonlinear Boltzmann cellular automata: Surface tension and wetting, *Phys. Rev. E* **51**, 3718 (1995).
- [73] S. Y. Chen, D. Martinez, and R. W. Mei, On boundary conditions in lattice Boltzmann methods, *Phys. Fluids* **8**, 2527 (1996).
- [74] A. Vian, V. Favrod, and E. Amstad, Reducing the shell thickness of double emulsions using microfluidics, *Microfluid. Nanofluid.* **20**, 159 (2016).
- [75] P. Sajeesh, M. Doble, and A. K. Sen, Hydrodynamic resistance and mobility of deformable objects in microfluidic channels, *Biomicrofluidics* **8**, 054112 (2014).
- [76] M. Zheng, Y. Ma, T. Jin, and J. Wang, Effects of topological changes in microchannel geometries on the asymmetric breakup of a droplet, *Microfluid. Nanofluid.* **20**, 107 (2016).